



Article

# Macrophages Loaded with Fe Nanoparticles for Enhanced Photothermal Ablation of Tumors

Lei Yu <sup>1</sup>, Shuntao Zhu <sup>2,3,4</sup>, Kun Qin <sup>1</sup> , Xueyu Fan <sup>1</sup> and Lu An <sup>2,3,4,\*</sup>

<sup>1</sup> Department of Dermatology, Zhujiang Hospital of Southern Medical University, No. 253 Gongye Avenue, Guangzhou 510282, China; xiaoyu927@smu.edu.cn (L.Y.); qinkun2022@foxmail.com (K.Q.); xueyufan2022@163.com (X.F.)

<sup>2</sup> The Key Laboratory of Resource Chemistry of the Ministry of Education, Shanghai Normal University, Shanghai 200234, China; shuntaozhu@163.com

<sup>3</sup> The Shanghai Key Laboratory of Rare Earth Functional Materials, Shanghai Normal University, Shanghai 200234, China

<sup>4</sup> The Shanghai Municipal Education Committee Key Laboratory of Molecular Imaging Probes and Sensors, Shanghai Normal University, Shanghai 200234, China

\* Correspondence: anlu1987@shnu.edu.cn

**Abstract:** Magnetic iron nanoparticle-based theranostics agents have attracted much attention due to their good magnetism and biocompatibility. However, efficiently enriching tumors with iron nanoparticles to enhance the treatment effect remains a pressing challenge. Herein, based on the targeting and high phagocytosis of macrophages, an Fe nanoparticle-loaded macrophage delivery system was designed and constructed to efficiently deliver iron nanoparticles to tumors. Hydrophilic Fe@Fe<sub>3</sub>O<sub>4</sub> nanoparticles with a core-shell structure were synthesized by pyrolysis and ligand exchange strategy. Subsequently, they were loaded into macrophages (RAW264.7 cells) using a co-incubation method. After loading into RAW264.7, the photothermal performance of Fe@Fe<sub>3</sub>O<sub>4</sub> nanoparticles were significantly enhanced. In addition, Fe@Fe<sub>3</sub>O<sub>4</sub> nanoparticles loaded into the macrophage RAW264.7 (Fe@Fe<sub>3</sub>O<sub>4</sub>@RAW) exhibited a good T<sub>2</sub>-weighted MRI contrast effect and clear tumor imaging in vivo due to the tumor targeting tendency of macrophages. More importantly, after being intravenously injected with Fe@Fe<sub>3</sub>O<sub>4</sub>@RAW and subjected to laser irradiation, the tumor growth was effectively inhibited, indicating that macrophage loading could enhance the tumor photothermal ablation ability of Fe@Fe<sub>3</sub>O<sub>4</sub>. The macrophage mediated delivery strategy for Fe@Fe<sub>3</sub>O<sub>4</sub> nanoparticles was able to enhance the treatment effect, and has great potential in tumor theranostics.

**Keywords:** iron magnetic nanoparticles; macrophages; nanoparticles delivery; photothermal therapy; MRI



**Citation:** Yu, L.; Zhu, S.; Qin, K.; Fan, X.; An, L. Macrophages Loaded with Fe Nanoparticles for Enhanced Photothermal Ablation of Tumors. *J. Funct. Biomater.* **2022**, *13*, 94. <https://doi.org/10.3390/jfb13030094>

Academic Editors: John H.T. Luong, Bella Manshian and Massimo Fresta

Received: 28 May 2022

Accepted: 12 July 2022

Published: 14 July 2022

**Publisher's Note:** MDPI stays neutral with regard to jurisdictional claims in published maps and institutional affiliations.



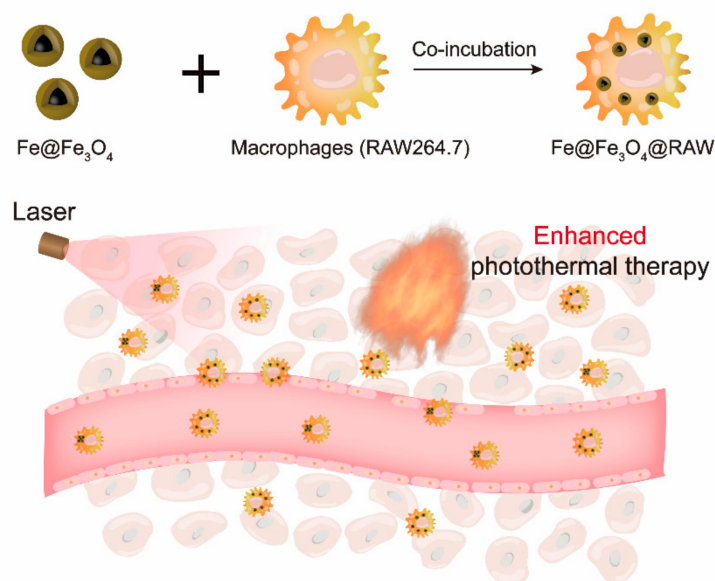
**Copyright:** © 2022 by the authors. Licensee MDPI, Basel, Switzerland. This article is an open access article distributed under the terms and conditions of the Creative Commons Attribution (CC BY) license (<https://creativecommons.org/licenses/by/4.0/>).

## 1. Introduction

Iron-based magnetic nanoparticles are considered excellent theranostics agents, which are widely used for tumor imaging and hyperthermia therapy due to their good biocompatibility and easy surface modification [1–5]. For example, iron-based nanoparticles are used in T<sub>2</sub>-weighted magnetic resonance imaging (MRI) and magnetic hyperthermia therapy due to their good magnetic properties, while their strong absorption in the near-infrared region also enables their use as good photoacoustic imaging and photothermal therapy agents [6–9]. A prerequisite for tumor theranostics is the efficient delivery of iron-based nanoparticles to tumors [10,11]. To date, a commonly used delivery strategy for iron-based nanoparticles is passive targeting delivery based on the enhanced permeability and retention (EPR) effect of tumors [12,13]. However, the delivery of iron-based nanoparticles based on the EPR effect is very easily obstructed by the reticuloendothelial system in vivo, resulting in the delivery efficiency of iron-based nanoparticles being very low [14,15]. Therefore, developing a new delivery strategy for iron-based nanoparticles to enhance the treatment effect of tumors is urgently required.

Cell-mediated nanoparticle delivery strategies have great potential in cancer theranostics, since they not only exhibit low biological toxicity but can also penetrate various biological barriers [16–20]. Among all the cells used for nanoparticle delivery, macrophages have attracted increasing attention due to two major advantages [21,22]. One is that macrophages can target cancer-related cytokines and chemokines, allowing them to specifically target and enrich tumors, and the other is that macrophages have a strong phagocytic ability, thus allowing them to load more nanoparticles compared with other cell carriers [23–25]. Therefore, macrophages are good candidate vehicles for the delivery of nanoparticles to cancer [26–28]. Based on this, Wang et al. reported that macrophages loaded with supramolecular aggregates of CuS nanoparticles can enhance tumor deposition and photothermal therapy [29]. Therefore, the macrophage-mediated delivery strategy will be ideal for the delivery of Fe nanoparticles; however, to the best of our knowledge, few references have been reported.

As a proof of concept, macrophages loaded with Fe-based nanoparticles were designed to demonstrate their enhanced photothermal therapy efficacy (Scheme 1). Firstly, hydrophobic Fe-based nanoparticles were prepared by a pyrolysis method. For bioapplications, the hydrophobic Fe nanoparticles required modification through ligand exchange to obtain hydrophilic Fe nanoparticles, which were subsequently loaded into macrophages (RAW264.7 cells) using a co-incubation method. Lastly, the photothermal and MRI performance of the RAW264.7 cells loaded with Fe nanoparticles were explored both in vitro and in vivo. This delivery strategy takes advantage of the targeting and high phagocytosis of macrophages, which can achieve the integration of tumor diagnosis and treatment, and has the potential to be applied to a variety of therapies.



**Scheme 1.** Macrophages loaded with Fe nanoparticles for an enhanced photothermal ablation of tumors.

## 2. Materials and Methods

### 2.1. Materials and Characterization

$\text{Fe}(\text{CO})_5$  was purchased from Kegonghua Chemical Technology Co., Ltd. (Beijing, China); 1-hexadecylamine, oleylamine and oleic acid were purchased from Sigma Aldrich (Taufkirchen, Germany); 1-octadecene and 3-(3,4-dihydroxyphenyl) propionic acid (DHCA) were obtained from Alfa Aesar (Lancashire, UK). All reagents (AR) were purchased and used directly without purification.

The crystalline phase of  $\text{Fe@Fe}_3\text{O}_4$  was analyzed by X-ray powder diffraction (XRD, D/MAX2000, Rigaku, Tokyo, Japan) and the morphology was characterized by transmission electron microscopy (TEM, JEM-2100, JEOL, Tokyo, Japan) and high-resolution

transmission electron microscopy (HR-TEM, JEM-2100, JEOL, Tokyo, Japan). The hydrodynamic size distribution and zeta potential of Fe@Fe<sub>3</sub>O<sub>4</sub> were determined by Zetasizer (Nano-ZS90, Malvern Panalytical, Malvern, UK). The functional groups existing on the surface of Fe@Fe<sub>3</sub>O<sub>4</sub> were characterized by Fourier transform infrared spectrum (FTIR, Nicolet-iS10, Thermo Fisher, Waltham, MA, USA). The absorbance of various concentrations of Fe@Fe<sub>3</sub>O<sub>4</sub> at 808 nm was measured by a UV spectrophotometer (DU 730, Beckman Coulter, Indianapolis, IN, USA). The concentration of Fe was determined by inductively coupled plasma-atomic emission spectrometry (ICP-AES, VISTAMPXICP Varian, Palo Alto, CA, USA). Temperature changes were recorded by a thermal camera (A310, FLIR Systems, Wilsonville, OR, USA), magnetic resonance imaging (MRI) in vitro and the relaxivity were obtained by a nuclear magnetic resonance imaging analyzer (0.5 T, NMI20-Analyst, NIUMAG, Shanghai, China), and MRI performed in vivo was characterized by a 1.0 T small animal MRI system (MesoMR, NIUMAG, Shanghai, China).

## 2.2. Synthesis of Fe@Fe<sub>3</sub>O<sub>4</sub> Nanoparticles

Hexadecylamine hydrochloride was prepared using an ice bath as described by [30]. Generally, hydrochloride was mixed with 1-hexadecylamine for 5 h until a white jelly was formed. After extraction with n-hexane and H<sub>2</sub>O, the product was filtrated and dried in a vacuum. The obtained hexadecylamine hydrochloride was mixed with 1-octadecene and oleylamine for 1 h under dehydrated and deoxygenated conditions at room temperature. This was then heated to 120 °C and continued to react for 40 min. Fe(CO)<sub>5</sub> was added to the high-temperature pyrolysis for 30 min at 185 °C. Subsequently, oleic acid was added for another 10 min, then the reaction was cooled down to room temperature. Finally, the hydrophobic Fe@Fe<sub>3</sub>O<sub>4</sub> was obtained after 1 h of air oxidation. The hydrophilic Fe@Fe<sub>3</sub>O<sub>4</sub> was synthesized by a ligand exchange method. Briefly, DHCA was mixed with hydrophobic Fe@Fe<sub>3</sub>O<sub>4</sub> in tetrahydrofuran for 2–3 h, then NaOH (0.5 M) was added, followed by washing with acetone and H<sub>2</sub>O and two rounds of centrifugation. The obtained hydrophilic Fe@Fe<sub>3</sub>O<sub>4</sub> nanoparticles were dispersed in H<sub>2</sub>O for subsequent use.

## 2.3. The Cytotoxicity Analysis

The RAW264.7 cell line was provided by the Cell Bank of Chinese Academy of Sciences (Shanghai, China). The cells in the logarithmic phase (10<sup>6</sup> cells) were incubated with different concentrations of Fe@Fe<sub>3</sub>O<sub>4</sub> nanoparticles (0, 10, 20, 50, 100, 200, 400, 600, 800, and 1000 µg/mL) for 24 h, then the supernatant was removed and the cells were washed with PBS. After that, the cell viability was determined according to a typical MTT assay (3-(4,5-dimethylthiazol-2-yl)-2,5-diphenyltetrazolium bromide) by the multi-mode microplate reader (Varioskan Flash, Thermo Fisher Scientific, Waltham, MA, USA).

For confocal imaging, RAW264.7 cells were seeded in a confocal petri dish. After the cells adhered to the dish, Fe@Fe<sub>3</sub>O<sub>4</sub> nanoparticles were added for co-incubation for 4 h, then the supernatant was removed and the cells were stained with Calcein-AM/PI live/dead double staining kit.

## 2.4. Construction of Fe@Fe<sub>3</sub>O<sub>4</sub>@RAW

The hydrophilic Fe@Fe<sub>3</sub>O<sub>4</sub> nanoparticles (1 mg/mL) were co-incubated with logarithmic macrophages (RAW264.7 cells, 10<sup>6</sup> cells) for 3 h, followed by the removal of the supernatant, and washing twice with PBS. After digestion by trypsin for 2 min, the suspension was centrifuged to collect Fe@Fe<sub>3</sub>O<sub>4</sub>@RAW. The Fe concentration was determined by ICP-AES.

## 2.5. MRI Analysis

The in vitro MRI, the longitudinal relaxation time ( $T_1$ ) and the transverse relaxation time ( $T_2$ ) of Fe@Fe<sub>3</sub>O<sub>4</sub>@RAW nanoparticles with different concentrations (0, 12.5, 25, 50, 100 and 200 µg/mL) were detected in a 0.5 T MRI analyzer. The parameters of  $T_2$ -weighted MRI were: TR = 2500 ms, TE = 36 ms, 82 × 120 mm, 220 Hz/Px. The longitudinal relaxivity

( $r_1$ ) and the transverse relaxivity ( $r_2$ ) were defined as the slope of the fitting line, with Fe concentration as the abscissa and  $1/T$  as the ordinate.

For in vivo MRI, the BALB/c mice were purchased from Shanghai SLAC Laboratory Animal Co., Ltd. (Shanghai, China). After intravenously injecting mice tumors with Fe@Fe<sub>3</sub>O<sub>4</sub>@RAW nanoparticles, MRI was performed in a 1.0 T MRI scanner at different times (0, 3, 5, and 7 h). The parameters of  $T_2$ -weighted MRI were: TR = 1500 ms, TE = 50 ms.

## 2.6. Characterization of Photothermal Properties

The Fe@Fe<sub>3</sub>O<sub>4</sub> suspension with different concentrations (0, 50, 100, 150 and 200 µg/mL) was irradiated with an 808 nm laser (1.0 W/cm<sup>2</sup>) for 900 s, and the temperature change was monitored by a photothermal imager. The photothermal conversion efficiency ( $\eta$ ) was calculated using:

$$\eta = \frac{hS(T_{max} - T_{surr}) - Q_{dis}}{I(1 - 10^{-A_{808}})} \quad (1)$$

where  $h$  is the heat conductivity,  $S$  is the surface area,  $T_{max}$  is the equilibrium temperature,  $T_{surr}$  is the initial temperature,  $Q_{dis}$  is the energy converted by water absorbing the light,  $I$  is the laser power of 808 nm, and  $A_{808}$  is the absorbance of Fe@Fe<sub>3</sub>O<sub>4</sub> at 808 nm.

The tumor growth was monitored for 16 days in 4T1 tumor-bearing mice. The mice were randomly divided into three groups (control, Fe@Fe<sub>3</sub>O<sub>4</sub> and Fe@Fe<sub>3</sub>O<sub>4</sub>@RAW), and were intravenously injected with PBS, Fe@Fe<sub>3</sub>O<sub>4</sub>, and Fe@Fe<sub>3</sub>O<sub>4</sub>@RAW, respectively. At 5 h after injection, the tumors in the right hind flank of the mice were subjected to laser irradiation (the laser irradiation distance was 1 cm, and the light spot area was 1.13 cm<sup>2</sup>), and then one mouse in each group was sacrificed and the tumor was collected for histopathological staining slices. The tumor growths of the other mice were monitored to investigate the photothermal therapy (PTT) effect.

## 2.7. Ethical Statement for the Tumor Model

The construction and use of the 4T1 tumor bearing model was approved by the Animal Ethics Committee of Shanghai Normal University and the guidelines of the Animal Protection and Animal Use Committee were strictly adhered to (22007066, January 2020).

## 2.8. Statistical Analyses

Data were analyzed with one-way ANOVA statistical analyses (multiple comparisons). Statistical significance was set at  $p < 0.05$  (\*  $p < 0.05$ , \*\*  $p < 0.01$ , \*\*\*  $p < 0.001$ ).

# 3. Results and Discussion

## 3.1. Synthesis and Characterization of Fe@Fe<sub>3</sub>O<sub>4</sub> Nanoparticles

The hydrophobic Fe-based nanoparticles (Fe@Fe<sub>3</sub>O<sub>4</sub>) were prepared following our previous report [31]. In order to improve their biocompatibility, hydrophilic Fe@Fe<sub>3</sub>O<sub>4</sub> nanoparticles were further synthesized by a ligand exchange strategy. Firstly, the crystal structure of the obtained Fe@Fe<sub>3</sub>O<sub>4</sub> nanoparticles was characterized by XRD (Figure 1a). The XRD pattern of the obtained Fe@Fe<sub>3</sub>O<sub>4</sub> exhibited two obvious peaks at 44.6° and 65.1° which matched well with the 110 and 200 crystal face of cubic Fe, respectively (JCPDS no. 6-0696). In addition, there were two weak peaks at 35.3° and 62.7°, which could be assigned to the 311 and 440 crystal face of cubic Fe<sub>3</sub>O<sub>4</sub>, respectively (JCPDS no. 1-1111). These results demonstrate that the obtained nanoparticles contained both Fe and Fe<sub>3</sub>O<sub>4</sub> crystals, and that the crystallinity of Fe was good, whereas that of Fe<sub>3</sub>O<sub>4</sub> was relatively poor. Further, the morphology of the obtained hydrophobic and hydrophilic Fe@Fe<sub>3</sub>O<sub>4</sub> nanoparticles was observed by TEM. As shown in Figure 1b, the obtained nanoparticles exhibited a core-shell structure with a core diameter of ~10 nm and a shell thickness of ~2 nm (Figure S1a), which can be more clearly observed in the HR-TEM image (Figure 1b inset). The inner core comprised the Fe nanoparticles, and the shell was the Fe<sub>3</sub>O<sub>4</sub> layer that prevented further oxidation of the Fe core, which was similar to previous results [32]. After ligand exchange (Figure 1c), the morphology and size (Figure S1b) did not change

significantly, and the core-shell structure could still be maintained (Figure 1c inset). Due to the presence of DHCA on the surface of Fe@Fe<sub>3</sub>O<sub>4</sub>, the hydrodynamic size was slightly higher than TEM, and the zeta potential was negative, which was consistent with previous results (Figure S2) [31]. Moreover, the two strong vibration peaks at 1575 cm<sup>-1</sup> and 1404 cm<sup>-1</sup> originated from the benzene ring of DHCA ligand, and the typical Fe-O stretching vibration peak appeared at 593 cm<sup>-1</sup> (Figure S3), indicating that the DHCA ligands were modified onto the Fe@Fe<sub>3</sub>O<sub>4</sub>. The above results demonstrate that the hydrophilic Fe@Fe<sub>3</sub>O<sub>4</sub> nanoparticles were prepared successfully.

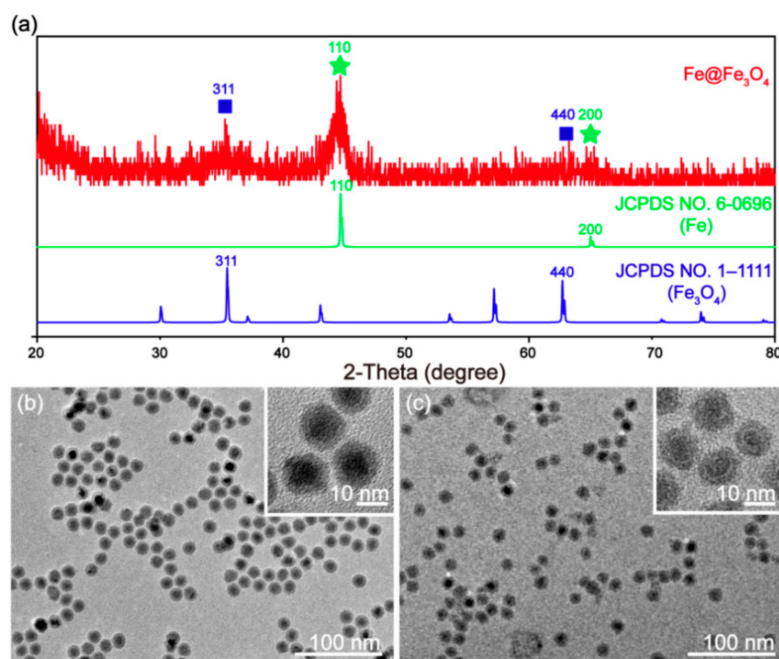


**Figure 1.** Characterization of Fe@Fe<sub>3</sub>O<sub>4</sub> nanoparticles. (a) XRD pattern of the obtained Fe@Fe<sub>3</sub>O<sub>4</sub> nanoparticles (red line) and the standard pattern of cubic Fe (green line, JCPDS no. 6-0696) and Fe<sub>3</sub>O<sub>4</sub> (blue line, JCPDS no. 1-1111). The stars and the squares indicate the characteristic peaks of Fe and Fe<sub>3</sub>O<sub>4</sub>, respectively. TEM and HR-TEM (inset) of the (b) hydrophobic and (c) hydrophilic Fe@Fe<sub>3</sub>O<sub>4</sub> nanoparticles.

### 3.2. Photothermal Performance of Fe@Fe<sub>3</sub>O<sub>4</sub> Nanoparticles

Considering that the photothermal performance of Fe@Fe<sub>3</sub>O<sub>4</sub> nanoparticles is related with their absorbance, the absorbance of various concentrations of Fe@Fe<sub>3</sub>O<sub>4</sub> was first explored (Figure S4a). As shown in Figure 2a, with the increasing concentration (50, 100, 150 and 200 µg/mL), the absorbance of Fe@Fe<sub>3</sub>O<sub>4</sub> nanoparticles at 808 nm gradually increased. In addition, compared with the control group (water), the temperature of the Fe@Fe<sub>3</sub>O<sub>4</sub> water dispersion increased dramatically after 808 nm irradiation (1.0 W/cm<sup>2</sup>), and when the concentration reached 100 µg/mL, the temperatures rose by more than 10 °C (Figures 2b and S4b), which was high enough for photothermal therapy (PTT). Moreover, in order to verify the photothermal stability of Fe@Fe<sub>3</sub>O<sub>4</sub> nanoparticles, the dispersion was irradiated for 15 min, then the irradiation was stopped to allow the sample to cool down to the initial temperature, followed by five cycles of re-irradiation. The heating effect and the maximum reachable temperature (Figure 2c) were essentially the same, indicating the good photothermal stability of the Fe@Fe<sub>3</sub>O<sub>4</sub> nanoparticles. The absorbance of the Fe@Fe<sub>3</sub>O<sub>4</sub> nanoparticles changed only slightly before and after laser irradiation (Figure S5), further demonstrating the good photothermal stability. The calculated photothermal conversion efficiency was 34.3% (Figure 2d), which is higher than typical Au nanorods (~22%) [33,34]. All of the above results demonstrate the good photothermal effect of Fe@Fe<sub>3</sub>O<sub>4</sub> nanoparticles.

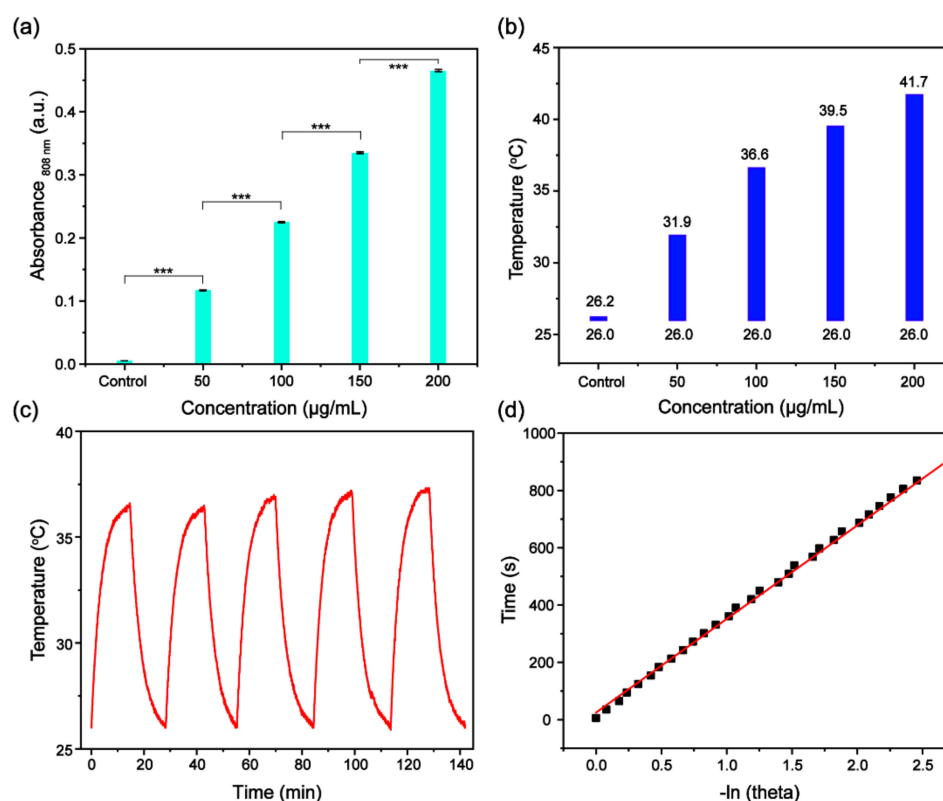


**Figure 2.** Photothermal performances of the Fe@Fe<sub>3</sub>O<sub>4</sub> nanoparticles. (a) Absorbance at 808 nm of water (control) and Fe@Fe<sub>3</sub>O<sub>4</sub> nanoparticles water dispersions of different concentrations. \*\*\*  $p < 0.001$ . (b) Increasing temperature of the water (control) and Fe@Fe<sub>3</sub>O<sub>4</sub> nanoparticle water dispersions of different concentrations under 808 nm laser irradiation. (c) Photothermal stability of the Fe@Fe<sub>3</sub>O<sub>4</sub> nanoparticle water dispersion under five cycles of laser on and off. (d) Time constant by applying the linear time data versus the negative natural logarithm of the driving force temperature (black square), which was obtained from (c).

### 3.3. Macrophages Loaded with Fe Nanoparticles

To explore the imaging and treatment effect of the Fe@Fe<sub>3</sub>O<sub>4</sub> nanoparticles delivered by macrophages, the MRI and photothermal performance in vitro should be explored. Before further investigation, the cytotoxicity of Fe@Fe<sub>3</sub>O<sub>4</sub> nanoparticles to RAW264.7 cells must first be confirmed. As an iron-based material, Fe@Fe<sub>3</sub>O<sub>4</sub> showed little toxicity, even at very high doses (Figure S6). Meanwhile, obvious green fluorescence (living cells) and weak red fluorescence (dead cells) were observed in the confocal images (Figure S7), indicating that Fe@Fe<sub>3</sub>O<sub>4</sub> nanoparticles had good biocompatibility. Based on this, RAW 264.7 phagocytic cells loaded with Fe@Fe<sub>3</sub>O<sub>4</sub> were constructed after 3 h of co-incubation (~717.1 pg/cell), and further irradiated with an 808 nm laser to investigate their photothermal performance (Figure S8). As expected, the macrophages loaded with Fe@Fe<sub>3</sub>O<sub>4</sub> (Fe@Fe<sub>3</sub>O<sub>4</sub>@RAW) exhibited a greater increase in temperature than the Fe@Fe<sub>3</sub>O<sub>4</sub> nanoparticles (Figure 3a). In contrast, the temperature of the control group (DMEM) containing cell medium only, barely increased, which ruled out the possibility of DMEM as a solvent interfering with the results. The greater heating effect may have been due to the aggregation of Fe@Fe<sub>3</sub>O<sub>4</sub> in the macrophages, resulting in locally concentrated heating [35]. Compared with previous reports, the macrophage loading strategy exhibited superior photothermal effect at lower laser power, while macrophages are shown to be excellent carriers for transporting Fe@Fe<sub>3</sub>O<sub>4</sub> to tumors [36,37]. Moreover, as for Fe@Fe<sub>3</sub>O<sub>4</sub>, after five cycles of laser on and off, the temperature rises of the Fe@Fe<sub>3</sub>O<sub>4</sub>@RAW dispersion remained stable (Figure 3b). All these results prove that Fe@Fe<sub>3</sub>O<sub>4</sub>@RAW is a potential PTT agent with good photothermal stability. Moreover, iron-based nanomaterials have been reported as magnetic resonance

imaging (MRI) contrast agents, thus  $T_2$ -weighted MRI of Fe@Fe<sub>3</sub>O<sub>4</sub>@RAW was investigated at 0.5 T field strength. As shown in Figure 3c, after being phagocytosed by RAW264.7 cells, Fe@Fe<sub>3</sub>O<sub>4</sub>@RAW with a lower concentration (0~50 µg/mL) exhibited  $T_2$ -enhanced contrast enhancement when the concentration was increased. When the concentration was greater than 50 µg/mL, the MR image was no longer darkened, which may have been due to phagocytic saturation of Fe@Fe<sub>3</sub>O<sub>4</sub> by RAW 264.7 cells. The transverse relaxivity ( $r_2$ ) and longitudinal relaxivity ( $r_1$ ) of Fe@Fe<sub>3</sub>O<sub>4</sub>@RAW were 55.513 mM<sup>-1</sup> s<sup>-1</sup> and 2.749 mM<sup>-1</sup> s<sup>-1</sup>, respectively (Figure 3d), which also indicated that it was a good  $T_2$  contrast agent. In addition,  $r_2$  of different patches of Fe@Fe<sub>3</sub>O<sub>4</sub>@RAW with the same Fe concentration was similar (Figure S9), indicating the good reproducibility of RAW loading Fe@Fe<sub>3</sub>O<sub>4</sub>. The above results demonstrate that macrophage phagocytosis could enhance the local aggregation of Fe@Fe<sub>3</sub>O<sub>4</sub>, thus enhancing the photothermal effect. Moreover, because of its good  $T_2$  MRI effect, Fe@Fe<sub>3</sub>O<sub>4</sub>@RAW can be used for MRI-mediated photothermal therapy.

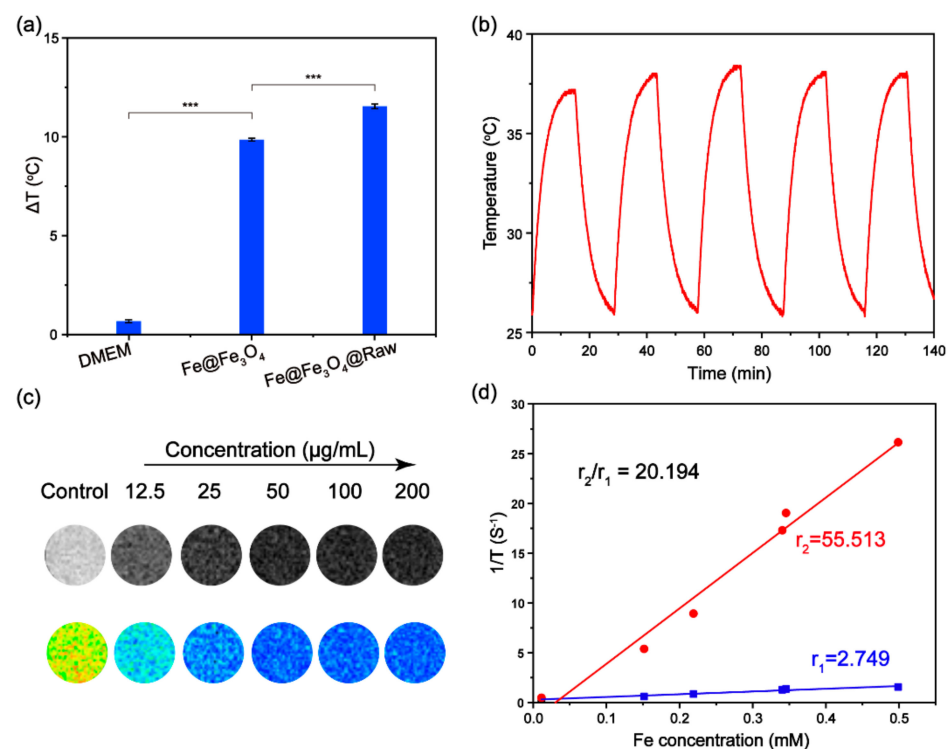


**Figure 3.** (a) Temperature changes ( $\Delta T$ ) of DMEM, Fe@Fe<sub>3</sub>O<sub>4</sub> nanoparticles (Fe@Fe<sub>3</sub>O<sub>4</sub>) and macrophages loaded with Fe@Fe<sub>3</sub>O<sub>4</sub> nanoparticles (Fe@Fe<sub>3</sub>O<sub>4</sub>@Raw) under 808 nm laser irradiation. \*\*\*  $p < 0.001$ . (b) Photothermal stability of the macrophages loaded with the Fe@Fe<sub>3</sub>O<sub>4</sub> nanoparticle water dispersion under the five cycles of laser on and off. (c)  $T_2$ -weighted MR images of water (control) and macrophages loaded with Fe@Fe<sub>3</sub>O<sub>4</sub> nanoparticles of different concentrations. (d) Transverse ( $r_2$ , red line) and longitudinal ( $r_1$ , blue line) relaxivity of the macrophages loaded with Fe@Fe<sub>3</sub>O<sub>4</sub> nanoparticles.

### 3.4. In Vivo Tumor MRI

Encouraged by the good  $T_2$  contrast effect of Fe@Fe<sub>3</sub>O<sub>4</sub>@RAW in vitro, the in vivo MRI performance was further explored in 4T1 tumor-bearing mice. As shown in Figure 4a, the tumor site (white circle) was darkened after intravenous injection of Fe@Fe<sub>3</sub>O<sub>4</sub>@RAW and continued to darken 5 h later, indicating the good  $T_2$ -weighted MRI contrast effect in vivo. The brightness gradually restored 7 h following injection, which may have been related to the metabolic character of Fe@Fe<sub>3</sub>O<sub>4</sub>@RAW. This suggested that Fe@Fe<sub>3</sub>O<sub>4</sub>@RAW can target the tumor and can be metabolized out of the body. The relative signal intensity at the tumor site can better reflect the changing trend of tumor imaging quantitatively (Figure 4b). The SNR% after intravenous injection of Fe@Fe<sub>3</sub>O<sub>4</sub>@RAW gradually decreased

until 5 h post-injection, then increased at 7 h post-injection, which further demonstrates that Fe@Fe<sub>3</sub>O<sub>4</sub>@RAW is a good targeted T<sub>2</sub>-weighted MRI contrast agent, and a benefit for tumor theranostics.

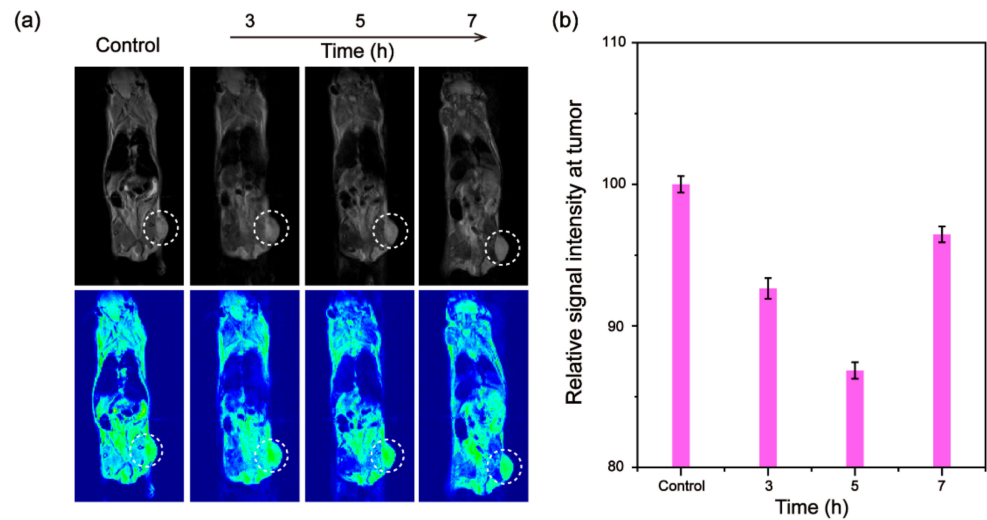


**Figure 4.** In vivo MRI performance. (a) T<sub>2</sub>-weighted MR images, and (b) corresponding relative signal intensity of tumor, before (control) and after intravenous injection of macrophages loaded with Fe@Fe<sub>3</sub>O<sub>4</sub> nanoparticles at different time points.

### 3.5. In Vivo Photothermal Tumor Ablation

As mentioned above, macrophage loading can enhance the photothermal effect of Fe@Fe<sub>3</sub>O<sub>4</sub> in vitro and exhibit tumor-targeting imaging effects, therefore, Fe@Fe<sub>3</sub>O<sub>4</sub>@RAW should be used as a tumor-targeting PTT agent. To prove this speculation, 4T1 tumor-bearing mice were randomly divided into three groups, including control, Fe@Fe<sub>3</sub>O<sub>4</sub> and Fe@Fe<sub>3</sub>O<sub>4</sub>@RAW groups, each of which was intravenously injected with PBS, Fe@Fe<sub>3</sub>O<sub>4</sub> and Fe@Fe<sub>3</sub>O<sub>4</sub>@RAW, respectively. Five hours after injection (the best accumulation time at the tumor site), all groups were irradiated with an 808 nm laser for 10 min. Subsequently, one mouse from each group was sacrificed and the tumor tissues were collected and stained with TdT-mediated DUTP Nick-End Labeling (TUNEL) and hematoxylin-eosin (H&E) for histopathological analysis. As shown in Figure 5, the apoptotic cells (brown) appeared in both the Fe@Fe<sub>3</sub>O<sub>4</sub> and Fe@Fe<sub>3</sub>O<sub>4</sub>@RAW groups, among which the apoptotic were more obvious (78.3%) in the Fe@Fe<sub>3</sub>O<sub>4</sub>@RAW group, demonstrating the more effective tumor PTT effect of Fe@Fe<sub>3</sub>O<sub>4</sub>@RAW. In contrast, after injection with PBS and laser irradiation, most of the cells were normal, indicating the safety of the laser. Similarly, in H&E tumor slices, the morphology of the cells in the Fe@Fe<sub>3</sub>O<sub>4</sub> and Fe@Fe<sub>3</sub>O<sub>4</sub>@RAW groups was destroyed, and the nucleus was absent, which further proves that the photothermal effect of Fe@Fe<sub>3</sub>O<sub>4</sub> is better after loading into macrophages.

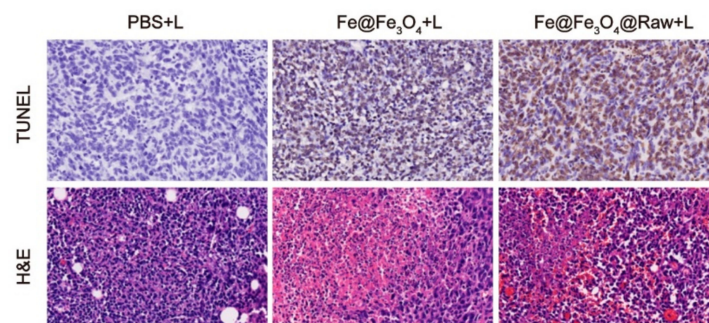


**Figure 5.** Tumor slice stained by TUNEL and H&E after photothermal therapy.

In addition, the remaining mice from each group were further monitored for 16 days after laser irradiation to evaluate the tumor therapeutic effect. As shown in Figure 6a, after laser irradiation, the tumor sites of the mice in the Fe@Fe<sub>3</sub>O<sub>4</sub> and Fe@Fe<sub>3</sub>O<sub>4</sub>@RAW groups were blackened, and the tumors were also ablated. However, the tumors in the Fe@Fe<sub>3</sub>O<sub>4</sub> group began to recur over time, while in the Fe@Fe<sub>3</sub>O<sub>4</sub>@RAW group, tumor growth was completely inhibited and the tumor site was scabbed. In comparison, the tumor growth in the PBS group was still fast, suggesting that the laser alone could not kill tumors. Meanwhile, the change of the relative tumor volume in the Fe@Fe<sub>3</sub>O<sub>4</sub>@RAW group was almost negligible, while that of the Fe@Fe<sub>3</sub>O<sub>4</sub> group showed a trend of slow growth, and that of the PBS group continued to grow (Figure 6b). Compared with the control group, the dissected tumors in the Fe@Fe<sub>3</sub>O<sub>4</sub> group were smaller after treatment. It is clear that part of the collected tumors from the Fe@Fe<sub>3</sub>O<sub>4</sub>@RAW group disappeared, meaning that the tumor was ablated and, although they existed, the tumors of the remaining mice were far smaller than those of the other two groups (Figure 6c). All these results further prove the good tumor inhibition effect of Fe@Fe<sub>3</sub>O<sub>4</sub>@RAW. Moreover, the body weight of mice in each group (Figure 6d) remained within a stable range during the treatment period, and no abnormal behavior was observed, which proved that Fe@Fe<sub>3</sub>O<sub>4</sub>@RAW and the laser were safe. This evidence indicates that Fe@Fe<sub>3</sub>O<sub>4</sub>@RAW is a potential PTT agent with good photothermal properties and low biological toxicity.

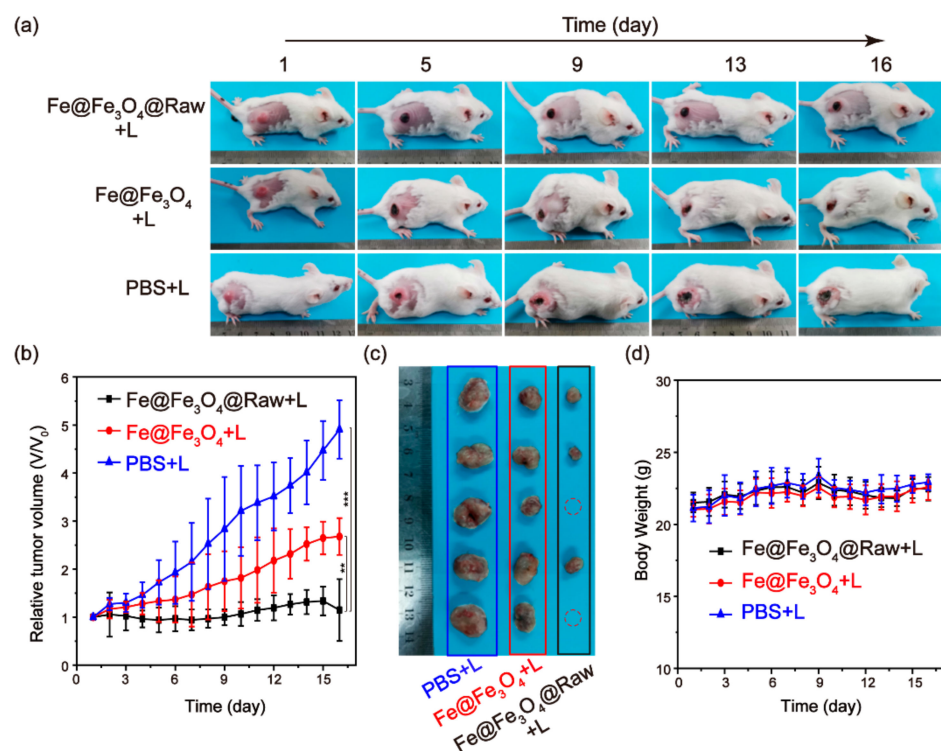


**Figure 6.** Photothermal therapy effects of the PBS, Fe@Fe<sub>3</sub>O<sub>4</sub>, and Fe@Fe<sub>3</sub>O<sub>4</sub>@RAW groups (n = 5). (a) Photographs of the mice in different groups on different days after photothermal therapy. (b) Relative tumor volume of the mice in the different groups after photothermal therapy (\*\* *p* < 0.01, \*\*\* *p* < 0.001). (c) Photographs of the dissected tumors 16 days after photothermal therapy. (d) Body weight of the mice in different groups after photothermal therapy.

#### 4. Conclusions

In summary, macrophages loaded with Fe@Fe<sub>3</sub>O<sub>4</sub> nanoparticles were constructed to enhance the photothermal ablation of tumors. Hydrophilic Fe@Fe<sub>3</sub>O<sub>4</sub> nanoparticles with a core-shell structure were synthesized by a pyrolysis and ligand exchange strategy. After loading into RAW264.7 cells, the local aggregation of Fe@Fe<sub>3</sub>O<sub>4</sub> nanoparticles resulted in an enhancement of the photothermal effect. In addition, Fe@Fe<sub>3</sub>O<sub>4</sub>@RAW exhibited a

good  $T_2$ -weighted MRI contrast effect and obvious tumor imaging in vivo due to the tumor targeting tendency of macrophages. More importantly, upon intravenous injection with Fe@Fe<sub>3</sub>O<sub>4</sub>@RAW and subjection to laser irradiation, tumor growth was inhibited effectively, indicating that macrophage loading could enhance the tumor photothermal ablation ability of Fe@Fe<sub>3</sub>O<sub>4</sub>. This delivery strategy takes advantage of the targeting and high phagocytosis of macrophages to achieve the integration of tumor diagnosis and treatment, and has the potential to be applied to a variety of therapies.

**Supplementary Materials:** The following supporting information can be downloaded at: <https://www.mdpi.com/article/10.3390/jfb13030094/s1>, Figure S1: Particle size statistics of Fe@Fe<sub>3</sub>O<sub>4</sub> nanoparticles; Figure S2: DLS and zeta potential of Fe@Fe<sub>3</sub>O<sub>4</sub>-DHCA; Figure S3: FTIR spectra of Fe@Fe<sub>3</sub>O<sub>4</sub> nanoparticles, DHCA and Fe@Fe<sub>3</sub>O<sub>4</sub>-DHCA; Figure S4: Absorbance and photothermal performance of hydrophilic Fe@Fe<sub>3</sub>O<sub>4</sub> nanoparticles; Figure S5: Absorbance of the Fe@Fe<sub>3</sub>O<sub>4</sub> nanoparticle before and after laser irradiation; Figure S6: The cytotoxicity; Figure S7: The confocal images stained with Calcein-AM/PI; Figure S8: Photothermal performance of DMEM, Fe@Fe<sub>3</sub>O<sub>4</sub> and Fe@Fe<sub>3</sub>O<sub>4</sub>@RAW under the irradiation of an 808 nm laser; Figure S9: The repeatability  $r_2$  of Fe@Fe<sub>3</sub>O<sub>4</sub>@RAW with same Fe concentration.

**Author Contributions:** Conceptualization, L.Y. and L.A.; data collecting and investigation, S.Z.; validation, K.Q. and X.F.; writing—original draft preparation, L.Y.; writing—review and editing, L.Y. and L.A. All authors have read and agreed to the published version of the manuscript.

**Funding:** This work was partially supported by the National Natural Science Foundation of China (22007066).

**Institutional Review Board Statement:** The animal study protocol was approved by the Ethics Committee of Shanghai Normal University (22007066, January 2020).

**Informed Consent Statement:** Not applicable.

**Data Availability Statement:** The data presented are available on request from the corresponding author.

**Conflicts of Interest:** The authors declare no conflict of interest.

## References

1. Ho, D.; Sun, X.; Sun, S. Monodisperse magnetic nanoparticles for theranostic applications. *Acc. Chem. Res.* **2011**, *44*, 875–882. [[CrossRef](#)] [[PubMed](#)]
2. Wang, J.; Mei, T.; Liu, Y.; Zhang, Y.; Zhang, Z.; Hu, Y.; Wang, Y.; Wu, M.; Yang, C.; Zhong, X.; et al. Dual-targeted and MRI-guided photothermal therapy via iron-based nanoparticles-incorporated neutrophils. *Biomater. Sci.* **2021**, *9*, 3968–3978. [[CrossRef](#)]
3. Alphanbéry, E. Light-interacting iron-based nanomaterials for localized cancer detection and treatment. *Acta Biomater.* **2021**, *124*, 50–71. [[CrossRef](#)] [[PubMed](#)]
4. Rajan, A.; Kaczmarek-Szczepańska, B.; Sahu, N.K. Magneto-thermal response of Fe<sub>3</sub>O<sub>4</sub>@CTAB nanoparticles for cancer hyperthermia applications. *Mater. Today Commun.* **2021**, *28*, 102583. [[CrossRef](#)]
5. Nicolás-Boluda, A.; Vaquero, J.; Laurent, G.; Renault, G.; Bazzi, R.; Donnadieu, E.; Roux, S.; Fouassier, L.; Gazeau, F. Photothermal depletion of cancer-associated fibroblasts normalizes tumor stiffness in desmoplastic cholangiocarcinoma. *ACS Nano* **2020**, *14*, 5738–5753. [[CrossRef](#)]
6. Qin, J.; Liu, Q.; Zhang, J.; Chen, J.; Chen, S.; Zhao, Y.; Du, J. Rationally separating the corona and membrane functions of polymer vesicles for enhanced  $T_2$  MRI and drug delivery. *ACS Appl. Mater. Interfaces* **2015**, *7*, 14043–14052. [[CrossRef](#)]
7. Zhou, P.; Zhao, H.; Wang, Q.; Zhou, Z.; Wang, J.; Deng, G.; Wang, X.; Liu, Q.; Yang, H.; Yang, S. Photoacoustic-enabled self-guidance in magnetic-hyperthermia Fe@Fe<sub>3</sub>O<sub>4</sub> nanoparticles for theranostics in vivo. *Adv. Healthc. Mater.* **2018**, *7*, 1701201. [[CrossRef](#)]
8. Atabaev, T.S. PEG-coated superparamagnetic dysprosium-doped Fe<sub>3</sub>O<sub>4</sub> nanoparticles for potential MRI imaging. *BioNanoScience* **2018**, *8*, 299–303. [[CrossRef](#)]
9. Nicolas-Boluda, A.; Laurent, G.; Bazzi, R.; Roux, S.; Donnadieu, E.; Gazeau, F. Two step promotion of a hot tumor immune environment by gold decorated iron oxide nanoflowers and light-triggered mild hyperthermia. *Nanoscale* **2021**, *13*, 18483–18497. [[CrossRef](#)]
10. Zhu, Y.; Fang, Y.; Kaskel, S. Folate-conjugated Fe<sub>3</sub>O<sub>4</sub>@SiO<sub>2</sub> hollow mesoporous spheres for targeted anticancer drug delivery. *J. Phys. Chem. C* **2010**, *114*, 16382–16388. [[CrossRef](#)]
11. Cheng, K.; Peng, S.; Xu, C.; Sun, S. Porous hollow Fe<sub>3</sub>O<sub>4</sub> nanoparticles for targeted delivery and controlled release of cisplatin. *J. Am. Chem. Soc.* **2009**, *131*, 10637–10644. [[CrossRef](#)] [[PubMed](#)]

12. Cai, H.; Li, K.; Shen, M.; Wen, S.; Luo, Y.; Peng, C.; Zhang, G.; Shi, X. Facile assembly of Fe<sub>3</sub>O<sub>4</sub>@Au nanocomposite particles for dual mode magnetic resonance and computed tomography imaging applications. *J. Mater. Chem.* **2012**, *22*, 15110–15120. [[CrossRef](#)]
13. Zhang, Y.; Li, X.; Zhang, Y.; Wei, J.; Wang, W.; Dong, C.; Xue, Y.; Liu, M.; Pei, R. Engineered Fe<sub>3</sub>O<sub>4</sub>-based nanomaterials for diagnosis and therapy of cancer. *New J. Chem.* **2021**, *45*, 7918–7941. [[CrossRef](#)]
14. Yu, M.; Zheng, J. Clearance pathways and tumor targeting of imaging nanoparticles. *ACS Nano* **2015**, *9*, 6655–6674. [[CrossRef](#)]
15. Wang, L.; Huang, J.; Chen, H.; Wu, H.; Xu, Y.; Li, Y.; Yi, H.; Wang, Y.A.; Yang, L.; Mao, H. Exerting enhanced permeability and retention effect driven delivery by ultrafine iron oxide nanoparticles with T<sub>1</sub>–T<sub>2</sub> switchable magnetic resonance imaging contrast. *ACS Nano* **2017**, *11*, 4582–4592. [[CrossRef](#)]
16. Xia, Y.; Rao, L.; Yao, H.; Wang, Z.; Ning, P.; Chen, X. Engineering macrophages for cancer immunotherapy and drug delivery. *Adv. Mater.* **2020**, *32*, 2002054.
17. Lang, T.; Dong, X.; Huang, Y.; Ran, W.; Yin, Q.; Zhang, P.; Zhang, Z.; Yu, H.; Li, Y. Ly6C<sup>hi</sup> monocytes delivering pH-sensitive micelle loading paclitaxel improve targeting therapy of metastatic breast cancer. *Adv. Funct. Mater.* **2017**, *27*, 1701093. [[CrossRef](#)]
18. Li, S.; Feng, S.; Ding, L.; Liu, Y.; Zhu, Q.; Qian, Z.; Gu, Y. Nanomedicine engulfed by macrophages for targeted tumor therapy. *Int. J. Nanomed.* **2016**, *11*, 4107–4124.
19. Feng, Y.; Liu, Q.; Li, Y.; Han, Y.; Liang, M.; Wang, H.; Yao, Q.; Wang, Y.; Yang, M.; Li, Z.; et al. Cell relay-delivery improves targeting and therapeutic efficacy in tumors. *Bioact. Mater.* **2021**, *6*, 1528–1540. [[CrossRef](#)]
20. Vercellino, S.; Kokalari, I.; Liz Cantoral, M.; Petseva, V.; Cursi, L.; Casoli, F.; Castagnola, V.; Boselli, L.; Fenoglio, I. Biological interactions of ferromagnetic iron oxide–carbon nanohybrids with alveolar epithelial cells. *Biomater. Sci.* **2022**, *10*, 3514–3526. [[CrossRef](#)]
21. Choi, J.; Kim, H.-Y.; Ju, E.J.; Jung, J.; Park, J.; Chung, H.-K.; Lee, J.S.; Lee, J.S.; Park, H.J.; Song, S.Y.; et al. Use of macrophages to deliver therapeutic and imaging contrast agents to tumors. *Biomaterials* **2012**, *33*, 4195–4203. [[CrossRef](#)] [[PubMed](#)]
22. Fu, J.; Wang, D.; Mei, D.; Zhang, H.; Wang, Z.; He, B.; Dai, W.; Zhang, H.; Wang, X.; Zhang, Q. Macrophage mediated biomimetic delivery system for the treatment of lung metastasis of breast cancer. *J. Control Release* **2015**, *204*, 11–19. [[CrossRef](#)] [[PubMed](#)]
23. An, L.; Wang, Y.; Lin, J.; Tian, Q.; Xie, Y.; Hu, J.; Yang, S. Macrophages-mediated delivery of small gold nanorods for tumor hypoxia photoacoustic imaging and enhanced photothermal therapy. *ACS Appl. Mater. Interfaces* **2019**, *11*, 15251–15261. [[CrossRef](#)] [[PubMed](#)]
24. Nguyen, V.D.; Min, H.-K.; Kim, H.Y.; Han, J.; Choi, Y.H.; Kim, C.-S.; Park, J.-O.; Choi, E. Primary macrophage-based microrobots: An effective tumor therapy in vivo by dual-targeting function and near-infrared-triggered drug release. *ACS Nano* **2021**, *15*, 8492–8506. [[CrossRef](#)] [[PubMed](#)]
25. Zhang, W.; Wang, M.; Tang, W.; Wen, R.; Zhou, S.; Lee, C.; Wang, H.; Jiang, W.; Delahunty, I.M.; Zhen, Z.; et al. Nanoparticle-laden macrophages for tumor-tropic drug delivery. *Adv. Mater.* **2018**, *30*, 1805557. [[CrossRef](#)] [[PubMed](#)]
26. Madsen, S.J.; Hirschberg, H. Macrophages as delivery vehicles for anticancer agents. *Ther. Deliv.* **2019**, *10*, 189–201.
27. Alvarenga, B.M.; Melo, M.N.; Frézard, F.; Demicheli, C.; Gomes, J.M.M.; Borba da Silva, J.B.; Speziali, N.L.; Corrêa Junior, J.D. Nanoparticle phosphate-based composites as vehicles for antimony delivery to macrophages: Possible use in leishmaniasis. *J. Mater. Chem. B* **2015**, *3*, 9250–9259. [[CrossRef](#)]
28. Burke, B.; Sumner, S.; Maitland, N.; Lewis, C.E. Macrophages in gene therapy: Cellular delivery vehicles and in vivo targets. *J. Leukoc. Biol.* **2002**, *72*, 417–428.
29. Li, J.; Cheng, Q.; Yue, L.; Gao, C.; Wei, J.; Ding, Y.; Wang, Y.; Zheng, Y.; Wang, R. Macrophage-hitchhiking supramolecular aggregates of CuS nanoparticles for enhanced tumor deposition and photothermal therapy. *Nanoscale Horiz.* **2021**, *6*, 907–912. [[CrossRef](#)]
30. Lacroix, L.-M.; Frey Huls, N.; Ho, D.; Sun, X.; Cheng, K.; Sun, S. Stable single-crystalline body centered cubic Fe nanoparticles. *Nano Lett.* **2011**, *11*, 1641–1645. [[CrossRef](#)]
31. Liu, D.; Li, J.; Wang, C.; An, L.; Lin, J.; Tian, Q.; Yang, S. Ultrasmall Fe@Fe<sub>3</sub>O<sub>4</sub> nanoparticles as T<sub>1</sub>–T<sub>2</sub> dual-mode MRI contrast agents for targeted tumor imaging. *Nanomed. NBM* **2021**, *32*, 102335. [[CrossRef](#)]
32. Zhou, Z.; Sun, Y.; Shen, J.; Wei, J.; Yu, C.; Kong, B.; Liu, W.; Yang, H.; Yang, S.; Wang, W. Iron/iron oxide core/shell nanoparticles for magnetic targeting MRI and near-infrared photothermal therapy. *Biomaterials* **2014**, *35*, 7470–7478. [[CrossRef](#)]
33. Chen, H.; Shao, L.; Ming, T.; Sun, Z.; Zhao, C.; Yang, B.; Wang, J. Understanding the photothermal conversion efficiency of gold nanocrystals. *Small* **2010**, *6*, 2272–2280. [[CrossRef](#)] [[PubMed](#)]
34. An, L.; Cao, M.; Zhang, X.; Lin, J.; Tian, Q.; Yang, S. pH and glutathione synergistically triggered release and self-assembly of Au nanospheres for tumor theranostics. *ACS Appl. Mater. Interfaces* **2020**, *12*, 8050–8061. [[CrossRef](#)] [[PubMed](#)]
35. Estelrich, J.; Busquets, M.A. Iron oxide nanoparticles in photothermal therapy. *Molecules* **2018**, *23*, 1567. [[CrossRef](#)] [[PubMed](#)]
36. Guo, X.; Wu, Z.; Li, W.; Wang, Z.; Li, Q.; Kong, F.; Zhang, H.; Zhu, X.; Du, Y.P.; Jin, Y.; et al. Appropriate size of magnetic nanoparticles for various bioapplications in cancer diagnostics and therapy. *ACS Appl. Mater. Interfaces* **2016**, *8*, 3092–3106. [[CrossRef](#)] [[PubMed](#)]
37. Shen, S.; Wang, S.; Zheng, R.; Zhu, X.; Jiang, X.; Fu, D.; Yang, W. Magnetic nanoparticle clusters for photothermal therapy with near-infrared irradiation. *Biomaterials* **2015**, *39*, 67–74.